Fayjaloun, R., Causse, M., Voisin, C., Cornou, C., Cotton, F. (2017): Spatial Variability of the Directivity Pulse Periods Observed during an Earthquake. - *Bulletin of the Seismological Society of America*, *107*, 1, pp. 308—318.

DOI: http://doi.org/10.1785/0120160199

THE SEISMOLOGICAL SOCIETY OF AMERICA
400 Evelyn Ave., Suite 201
Albany, CA 94706-1375
(510) 525-5474; FAX (510) 525-7204
www.seismosoc.org

Bulletin of the Seismological Society of America, Vol. 107, No. 1, pp. 308–318, February 2017, doi: 10.1785/0120160199

Spatial Variability of the Directivity Pulse Periods Observed during an Earthquake

by Rosemary Fayjaloun, Mathieu Causse, Christophe Voisin, Cecile Cornou, and Fabrice Cotton

Abstract The ground velocity pulses generated by rupture directivity effects in the near-fault region can cause a large amount of damage to structures. Proper estimation of the period of such velocity pulses is of particular importance in characterizing near-fault seismic hazard and mitigating potential damage. We propose a simple equation to determine the pulse period as a function of the site location with respect to the fault rupture (defined by the hypocentral distance *hypD*, the closest distance to the rupture area *clsD*, and the length of the rupture area that breaks toward the site *D*) and some basic rupture properties (average rupture speed and average rise time). Our equation is first validated from a dataset of synthetic velocity time histories, deploying simulations of various strike-slip extended ruptures in a homogeneous medium. The analysis of the synthetic dataset confirms that the pulse period does not depend on the whole rupture area, but only on the parameter *D*. It also reveals that the pulse period is not sensitive to the level of slip heterogeneity on the fault plane. Our model is tested next on a real dataset build from the Next Generation Attenuation-West2 Project database, compiling 110 observations of velocity pulse periods from 10 strike-slip events and 6 non-strike-slip events. The standard deviation of the natural logarithm residuals between observations and predictions is ∼0.5. Furthermore, the correlation coefficient between observations and predictions equals ∼0.8, indicating that despite its simplicity, our model explains fairly well the spatial variability of the pulse periods.

Introduction

The directivity of the earthquake rupture propagation gives rise to a large variability of the ground motions recorded at a given distance from the source over various source–receiver azimuths (e.g., Somerville *et al.*, 1997; Spudich and Chiou, 2008). In particular, the energy of the seismic waves successively released from the fault constructively interferes in the forward direction of the rupture, which makes the amplitude of the ground shaking large, especially when the rupture speed approaches the shear-wavespeed. This results in a large amplitude *S* wave, called the "pulse". Such pulses are essentially observed in case of forward directivity and in the near-fault region, the probability that ground velocity is pulse-like being maximum at the vicinity of the rupture termination (Shahi and Baker, 2011; see also Fig. 1). The pulse is of particular interest from a structural earthquake-engineering point of view, because the demand on the structure is amplified when the natural period of the structure equals the pulse period (e.g., Biggs, 1964; Veletsos *et al.*, 1965; Anderson and Bertero, 1987; Hall *et al.*, 1995). In particular, the pulse period has been shown to be a critical parameter for design spectra, strength-reduction factors, damping modification factors, residual displacements, and ductility demands (Alavi and Krawinkler, 2001; Mavroeidis *et al.*, 2004; Hubbard and Mavroeidis, 2011; Ruiz-Garcia, 2011; Liossatou and Fardis, 2016). Accurate predictions of directivity pulse periods are then crucial for near-fault seismic risk assessment. Several studies showed that the pulse period scales with moment magnitude, and proposed empirical relationships to relate the pulse period to earthquake magnitude (e.g., Somerville, 1998, 2003; Mavroeidis and Papageorgiou, 2003; Bray and Rodriguez-Marek, 2004; Shahi and Baker, 2011). Recently, Cork *et al.* (2016) claimed that the pulse period may be related to other source features, such as the tectonic regime or the stress drop.

In this article, we investigate the spatial dependency of the pulse period and its dependency on some basic parameters describing the rupture process. We propose that the pulse period can be approximated from a simple equation including the relative location of the observation points with respect to the rupture (*D*, *clsD*), the ratio between the rupture speed and the shear-wavespeed (V_r/V_S), and the duration of the local slip (T_{rise}). Our simple model is first validated on a synthetic dataset based on simulations of extended strike-slip ruptures. The model is then compared with the real data

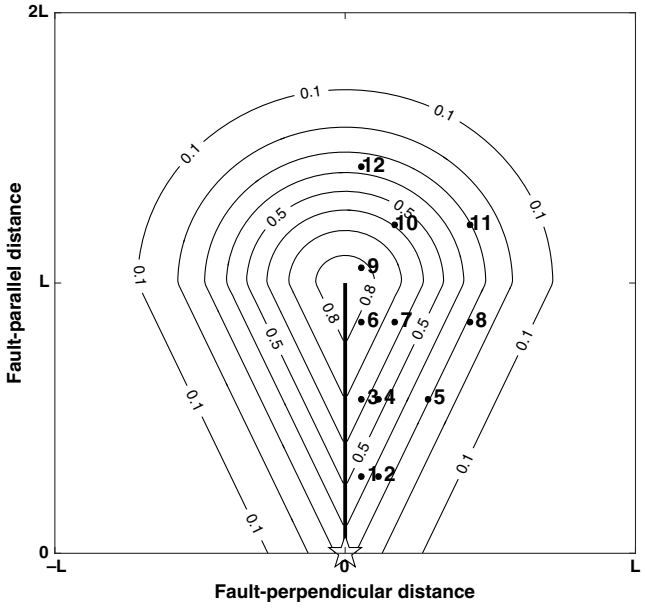

Figure 1. Distribution of the stations with respect to the top-fault rupture projection for the synthetic dataset of strike-slip rupture simulations. The black lines represent iso-values of the probability to observe a pulse, as given by Shahi and Baker (2011, their equation 6).

selected from the Next Generation Attenuation-West2 Project (NGA-West2) database, compiling 110 observations of pulses periods from 10 strike-slip events and 6 non-strike-slip events.

Relationship between Pulse Period, Rupture Parameters, and Station Position based on Analysis of Synthetic Velocity Time Series

Simulation of Velocity Time Series

First, we simulate a suite of velocity time series for vertical strike-slip ruptures in a homogeneous medium at a set of 12 stations (Fig. 1). The stations are located in the near-fault region (distance from the surface fault projection is smaller than half the rupture length). The rupture initiates at one edge of the fault and propagates at a constant rupture velocity, so that each station sees part or the totality of the rupture arriving. For comparison, Figure 1 displays the contour lines of the probability that the observed velocity is pulse-like, as computed by the Shahi and Baker (2011) empirical equation, derived from a real dataset of strike-slip velocity time series. The Green's functions are computed using the discrete wavenumber technique (Bouchon, 1981), up to a frequency of 3 Hz, considering a shear-wave velocity $V_S = 3$ km/s. The rupture area is 40×14 km^2 and the average slip is 1 m, so that the simulated ruptures correspond to $M \sim 6$. The rise time (i.e., the local slip duration) and the final slip are assumed to be constant over the fault plane. In order to analyze the effect of slip heterogeneity, we also consider heterogeneous slip distributions (Fig. 2a). Those distributions are generated assuming a k^{-2} slope in the wavenumber domain beyond a corner wavenumber k_c (e.g., Causse *et al.*, 2009). The inverse of k_c is proportional to the slip correlation length (characteristic size of slip heterogeneity), whereas the level of the high-frequency slip spectrum is related to the standard deviation of slip (amplitude of slip heterogeneity). The value of the pulse period T_p is computed next using the algorithm developed by Baker (2007), based on continuous wavelet transform. The pulse period is equal to the period of the wavelet associated with the largest coefficient, considering Daubechies wavelet of order 4 as a mother wavelet. Note that the Baker (2007) algorithm is used here for the sake of consistency, because it has been used to complete the NGA-West2 database analyzed in the Comparison between Predicted Pulse Period (Equation 1) and Real Observations (NGA-West2 Database) section.

Figure 2b displays the fault-normal components of the simulated velocity at station 4 (left) and the corresponding extracted pulses (right) for constant or heterogeneous slip distributions. The result indicates that the pulse period is not sensitive to the level of heterogeneity. Figure 2b also shows that considering the whole rupture area or only the area defined by the rectangle (Fig. 2a) does not modify the velocity pulse. The only noticeable difference between the two synthetics is a more pronounced stopping phase when the rupture is shortened and stops aside the station. This clearly illustrates that the pulse essentially arises from a coherent summation of waves emitted by the fault area that ruptures toward the site. This is also pointed out by Mavroeidis and Papageorgiou

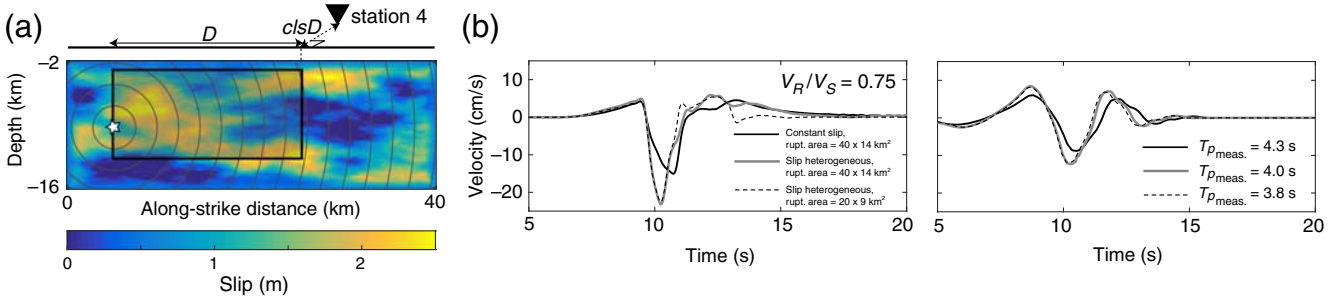

Figure 2. (a) Description of the rupture propagation. Slip is supposed to be constant on the fault plane (equal to 1 m) or heterogeneous. The displayed slip distribution has a correlation length of 20 km along strike and 7 km along dip, and has a standard deviation of 0.75 m. The white star represents the rupture initiation. The rupture speed is constant. (b, left) Simulated velocity at station 4 (fault-normal component) for homogeneous or heterogeneous rupture, or considering the rupture area represented by the rectangle in (a). (b, right) Extracted pulses and values of the pulse periods using the Baker (2007) algorithm at station 4. The color version of this figure is available only in the electronic edition.

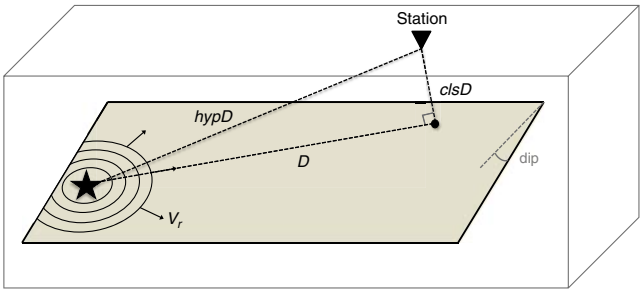

Figure 3. Illustrative scheme describing the parameters used in equation (1). *HypD* denotes the hypocentral distance, *clsD* denotes the closest distance to the rupture area, *D* denotes the length of the rupture area that breaks toward the site, and V_r is the rupture velocity. The color version of this figure is available only in the electronic edition.

(2010), who used the concept of isochrones to relate the characteristics of near-fault directivity pulses to the rupture properties. They showed that velocity pulses observed at stations located close to the fault surface projection are associated with a fault area of large isochrones velocities, which extends from the hypocenter to the top of the fault.

Simple Relationship between Pulse Period, Rupture Parameters, and Station Position

Based on the previous analysis, we propose that the pulse period can be approximated by the following simple equation:

$$T_{\text{pulse}} = \left(\frac{D}{V_r} + \frac{clsD}{V_s} - \frac{hypD}{V_s}\right) + T_{\text{rise}}, \qquad (1)$$

in which D is the length of the fault area that ruptures toward the site, measured between the hypocenter, and the closest point from the fault to the site, *clsD* is the closest distance from the recorded site to the ruptured fault area, and *hypD* is the hypocentral distance (as shown in Fig. 2a). Those parameters are illustrated in a more general case (for any fault mechanism) in Figure 3. Note that equation (1) is valid for subshear ruptures only, that is, when the ratio between the rupture speed and the shear-wave velocity V_r/V_S is smaller than 1.

To test the robustness of this simple approximation, we compare the pulse-period values extracted from our simulations using the wavelet algorithm (Baker, 2007) with the values obtained from equation (1), for different values of V_r/V_S and T_{rise} at the whole set of stations (Fig. 4). The standard deviation of the natural logarithm residuals equals 0.27, and the coefficient of correlation between observations and predictions equals 0.91, indicating that equation (1) provides a fairly good approximation of the pulse period. However, because the shape of the considered wavelet does not systematically match the shape of the synthetic velocity pulses, equation (1) sometimes underestimates the pulse periods obtained from the wavelet algorithm. This is the case for stations located next to or beyond the rupture termination (stations 6, 7, 9, 10, and 12) and when the V_r/V_S ratio is lower than ~0.8. This is illustrated in Figure 5, showing that the duration of the synthetic velocity pulse at station 12, well delimited by the first *S*-wave arrival and a stopping phase, is well predicted by equation (1). Nevertheless, the wavelet used to approximate the pulse has a significantly larger period. This raises the question of the real meaning of the pulse period, its relation to the pulse duration, and how to properly measure it. Recently, Cork *et al.* (2016) pointed out that the use of various techniques can result in significantly different values of the pulse period. This issue remains, however, beyond the scope of this study.

Comparison between Predicted Pulse Period (Equation 1) and Real Observations (NGA-West2 Database)

Data Selection

To test equation (1) with real data, we refer to the NGA-West2 database. Earthquake data are selected based on the availability of the velocity pulse period and the rupture parameter values. The source parameters of the considered events are reported in Table 1. Two additional earthquakes, not fully described in the database, are included in our dataset: (1) the 2003 Bam, Iran, earthquake and (2) the 2004 Parkfield,

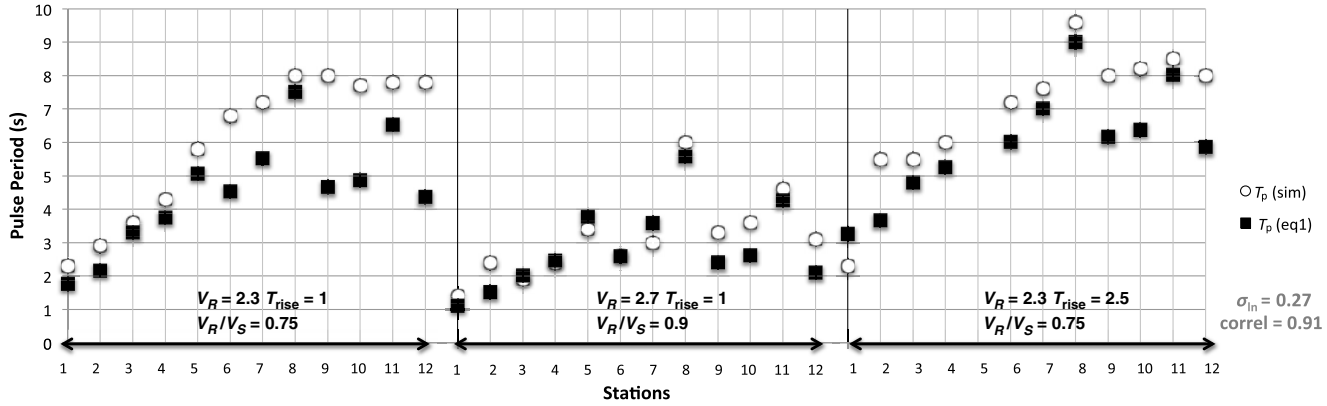

Figure 4. Values of the synthetic velocity pulse periods at the 12 stations for three different rupture scenarios with uniform slip. The circles represent the extracted pulse periods using the wavelet approach (Baker, 2007), denoted by T_p (sim), and the filled squares represent the calculated pulse periods using equation (1), denoted by T_p (eq1).

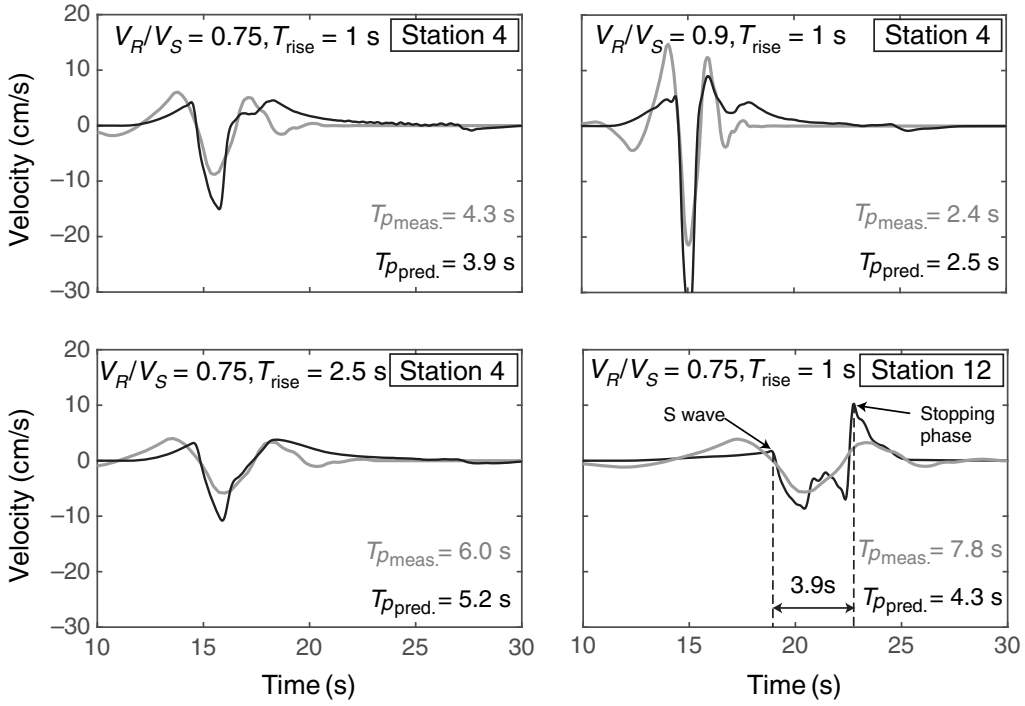

Figure 5. Simulated velocity time series (black line) (fault-normal component) and extracted pulses (gray line) using the Baker (2007) algorithm. The slip is assumed to be constant over the fault plane. $T_{p_{meas.}}$ denotes the period of the extracted pulse, whereas $T_{p_{pred.}}$ denotes the pulse period predicted from equation (1).

California, earthquake. For the Bam earthquake, rupture parameters are determined from the study by Bouchon *et al.* (2006). For the Parkfield event, we refer to Twardzik *et al.* (2012) for the V_r and V_S values. Furthermore, according to Custodio *et al.* (2005), we choose $T_{\text{rise}} = 0.88$ s. The latter parameters are emphasized in italics in Table 1 and the information about each station (velocity pulse period and station position) can be found in the Appendix.

Results

Figure 6 displays the values of the extracted (T_p (NGA)) and the calculated (T_p (eq1)) velocity pulse periods at all the

Table 1
List of Earthquakes Considered in the Present Study

Earthquakes	Year	M_w*	$L^\dagger$	$T_{\text{rise}}^\ddagger$	$V_r^\S$	$V_r/V_S^\parallel$	Stations	
Coyote Lake	1979	5.74	6.6	0.43	2.68	0.77	4	SS
Parkfield	2004	6.00	40	*0.88*	*2.7*	*0.8*	11	SS
Morgan Hill	1984	6.19	27	0.43	2.58	0.80	2	SS
Imperial Valley	1979	6.53	50	0.87	2.70	0.87	12	SS
Superstition Hills	1987	6.54	20	0.62	2.47	0.77	2	SS
Bam, Iran	2003	6.60	15	*1.40*	*2.80*	*0.92*	1	SS
Kobe, Japan	1995	6.90	60	1.24	2.68	0.80	5	SS
Duzce, Turkey	1999	7.14	46.8	1.90	2.80	0.80	2	SS
Landers	1992	7.28	71.8	2.90	2.76	0.78	3	SS
Kocaeli, Turkey	1999	7.51	137.5	2.60	2.95	0.80	4	SS
San Fernando	1971	6.61	20	1.02	2.53	0.78	1	N-SS
Northridge	1994	6.69	18	1.15	2.90	0.81	14	N-SS
Loma Prieta	1989	6.93	40	1.50	2.79	0.77	6	N-SS
Cape Mendocino	1992	7.01	20	1.40	2.56	0.80	3	N-SS
Tabas, Iran	1978	7.35	90	3.22	2.51	0.80	1	N-SS
Chi-Chi, Taiwan	1999	7.62	88	3.30	2.80	0.80	39	N-SS

SS, Strike slip; N-SS, non-strike slip.
*Earthquake magnitude.
†Fault length in kilometers.
‡Rise time in seconds.
§Rupture speed in kilometers per second.
‖Ratio between the rupture speed and the shear wavespeed.

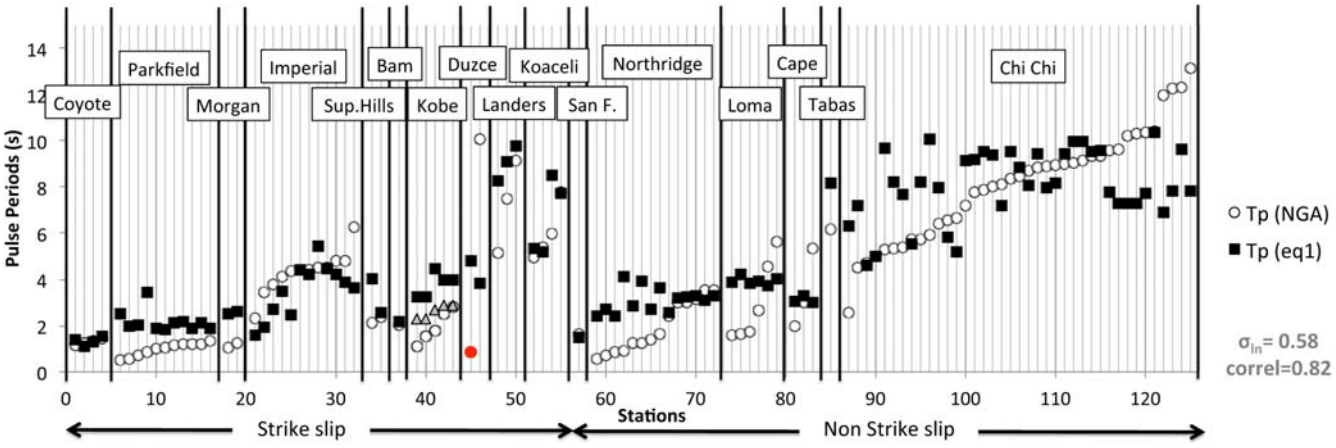

Figure 6. Database of pulse periods from 16 different earthquakes at 110 stations. The circles represent the extracted pulse periods using the wavelet approach of Baker (2007) as listed in the Next Generation Attenuation-West2 Project (NGA-West2) database, denoted by T_p (NGA), and the filled squares represent the calculated pulse periods using equation (1), denoted by T_p (eq1). The color version of this figure is available only in the electronic edition.

stations. It illustrates the large variability of the recorded pulse period for a given earthquake. To quantify the misfit between the observations and the predictions, we compute the standard deviation of the natural logarithm residuals. We obtain $\sigma_{\ln T} = 0.58$ using the whole dataset. Furthermore, we note that the distribution of the natural logarithm residuals is not centered around 0 but around 0.2, which means that equation (1) slightly overestimates the observed T_p (NGA) values ($\sim +20\%$). One possible explanation is that the pulse period may be controlled by asperity dimensions, which are typically less than the distance D used in equation (1). This potential behavior is not captured by our k^{-2} heterogeneous rupture simulations, which show that the pulse period is almost insensitive to the level of slip heterogeneity, but may be revealed by more complex (nonstationary) slip distributions. Finally, the correlation coefficient between the predicted and the observed pulse periods is corr = 0.82, indicating that even if significant discrepancies can be observed for certain events, equation (1) explains most of the spatial variability of the pulse period.

The largest discrepancies are observed at some of the stations that recorded the 1994 Northridge earthquake, for which equation (1) overestimates the pulse period by a factor larger than 4. These large discrepancies may be explained by the simplicity of equation (1), in which the source process is modeled by means of a single fault plane. Using teleseismic waveform inversion and analysis of aftershock distribution, Thio and Kanamori (1996) showed that the 1994 Northridge rupture was complex, consisting of three subevents that ruptured with a time-shift of about 2 s.

We also note that equation (1) overestimates the pulse period for the 1995 Kobe earthquake (by a value of about 2 s). This arises because the average rupture speed of 2.7 km/s provided in the NGA-West2 database may be underestimated.

Table 2 lists the rupture speed values as reported by several published finite-source inversion models (available at Finite-Source Rupture Model Database [SRCMOD database], Mai and Thingbaijam, 2014), indicating the rupture speed is probably closer to 3 km/s. Using $V_r = 0.9$ and $V_S = 3.1$ km/s (e.g., Guo *et al.*, 2013) results in a better fit with observations, as indicated by triangles in Figure 6.

Finally, the pulse period observed at station BOL during the 1999 Duzce earthquake (Fig. 6, filled circle) is strongly overestimated. This may arise because the V_r/V_S value reported in the NGA-West2 database is 0.8, whereas the rupture toward station BOL propagated at a supershear speed (i.e., $V_r/V_S > 1$; Bouchon *et al.*, 2010). As reported in several studies (e.g., Bernard and Baumont, 2005), supershear ruptures are associated with a shock wave propagating in the near-source region called Mach front. This shock wave is characterized by a pulse of large amplitude and a short duration. Note that supershear rupture was also observed for the 1999 Koaceli earthquake, but on a fault segment that ruptured beyond the four stations considered in our study (Arcelik, Gebcze, İzmit, and Yarimca; Bouchon *et al.*, 2010). Thus, these four stations were not affected by the Mach front.

After screening out the data from the Northridge and the Duzce earthquakes, and considering $V_r/V_S = 0.9$ for the Kobe earthquake, the value of $\sigma_{\ln T}$ drops from 0.58 to 0.47

Table 2
Rupture Speed Values for the 1995 Kobe Earthquake According to Various Published Source Models

Source Model Reference for the Kobe Earthquake	V_r*
Zeng and Anderson (2000)	2.8
Yoshida *et al.* (1996)	2.5
Wald (1996)	2.8
Koketsu *et al.* (1998)	2.5
Ide *et al.* (1996)	3
Horikawa *et al.* (1996)	3
Cho and Nakanishi (2000)	3.4
Guo *et al.* (2013)	3.1
Sekiguchi *et al.* (2000)	3.1

*Rupture speed in kilometers per second.

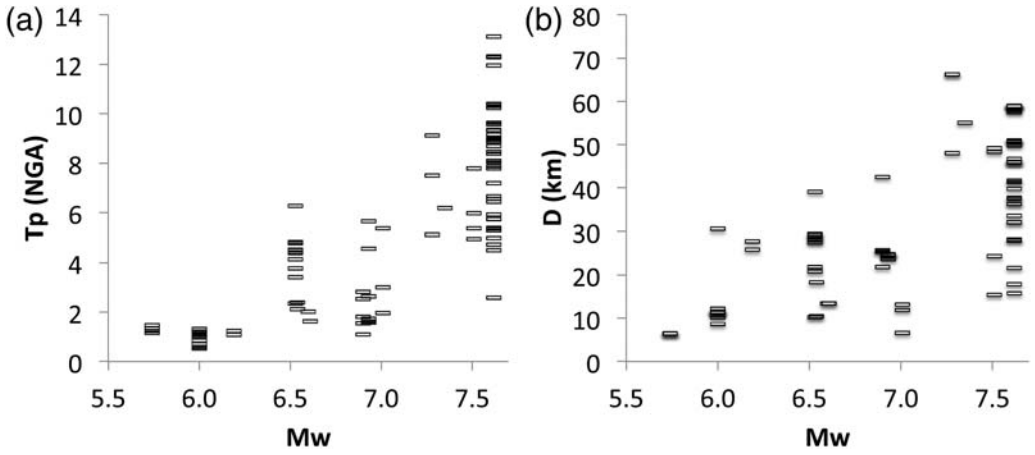

Figure 7. (a) D as a function of moment magnitude for the NGA-West2 dataset considered in this study (see the Appendix). (b) Value of the pulse period T_p (NGA) as a function of moment magnitude.

considering the whole dataset, from 0.63 to 0.55 considering strike-slip earthquakes only, and from 0.52 to 0.38 for non-strike-slip earthquakes. The correlation coefficient remains almost unchanged (corr = 0.84), however. Separating the events according to their mechanism, we obtain $\text{corr}_{SS} = 0.86$ for strike-slip events and $\text{corr}_{N-SS} = 0.68$ for non-strike-slip events. This seems to indicate that although the $\sigma_{\ln T}$ is smaller for non-strike-slip events, equation (1) still better predicts the spatial variability of the pulse period for strike-slip events.

Discussion

Several studies proposed empirical models relating the pulse period to earthquake magnitude, assuming a linear relationship between $\log(T_p)$ and M (e.g., Somerville, 2003; Shahi and Baker, 2011; Cork *et al.*, 2016). All these models show evidence of an increase of T_p with M. Note that our model (equation 1) does not include magnitude or seismic moment explicitly (or any parameter that scales with seismic moment like average slip or rupture length). The increase of T_p with M is, however, implicitly expressed through the parameter D (length of the fault area rupturing toward a given station). This is simply because, as magnitude increases, the length of the rupture increases, and therefore the range of potential values of D, and hence Tp, also increases (as shown in Fig. 7a). Figure 7b clearly indicates that the T_p values follow a similar trend, and that large events can also have small T_p values. Thus, our model provides a simple physical basis to explain how T_p is linked to magnitude.

Although $T_p - M$ empirical models give a practical and direct way to predict T_p for a potential scenario earthquake, our approach requires the knowledge of some rupture parameters (rupture velocity and rise time). Though these parameters only describe the basic features of the rupture propagation,

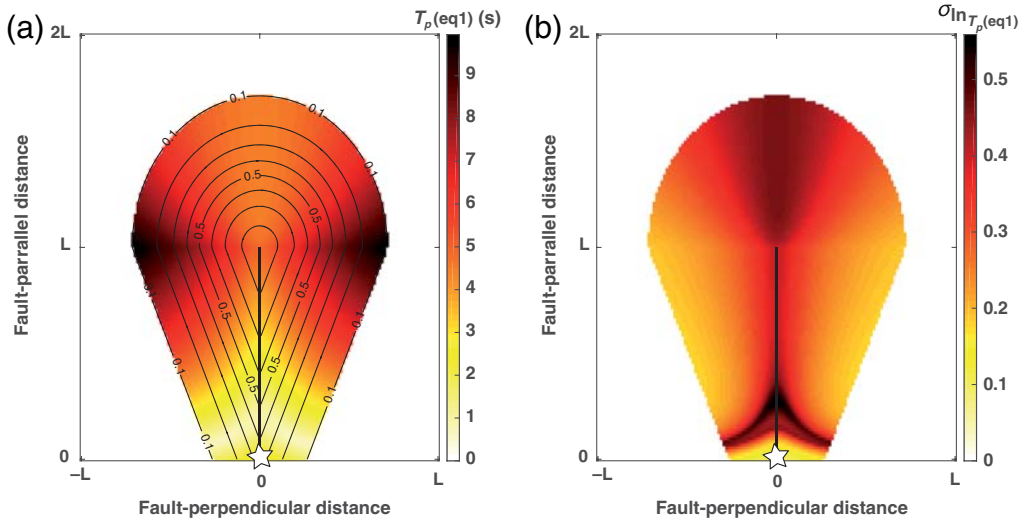

Figure 8. (a) Spatial distribution of the mean pulse-period value and (b) standard deviation of the natural logarithm pulse periods for V_r/V_S and T_{rise} following a uniform distribution in the range [0.6–0.9] and [0.1–1], respectively. The thin black lines in (a) represent the isovalues of the probability to observe a velocity pulse, as defined by Shahi and Baker (2011). The star represents the hypocenter and the thick black line represents the fault surface projection. The color version of this figure is available only in the electronic edition.

they remain difficult to predict *a priori*. After Heaton (1990) and Somerville *et al.* (1999), the values of the V_r/V_S ratio observed for most ruptures are in the range [0.6–0.9]. The rupture velocity can also vary locally within a single rupture (e.g., Archuleta, 1984). To quantify the variability of the velocity pulse period that would be predicted from equation (1) for a future earthquake, we compute T_p for 10,000 rupture scenarios for an M 6 strike-slip rupture (Fig. 2a). We assume that the V_r/V_S ratio is uniformly distributed in the range [0.6–0.9]. We also assume that the rise-time values are uniformly distributed in the range [0.1–1]. Figure 8a and 8b represents the spatial distribution of the mean pulse period and logarithm standard deviation, respectively. Standard deviation varies from 0.09 to 0.56, depending on the location of the station with respect to the fault. Overall, stations located close to the fault surface projection or beyond the fault termination are more sensitive to uncertainties in the source parameters. The highest uncertainty is observed at some specific locations at the vicinity of the hypocenter, for which the pulse period equals the smallest possible value (i.e., the rise-time value). The pulse-period uncertainty is then directly controlled by the rise-time uncertainty.

To reduce uncertainty in the pulse-period predictions for a potential future event, it is then essential to constrain the range of physically realistic rupture-parameter values. Some studies established links between the rupture speed and some fault properties or other physical parameters describing the rupture, which may help in refining the *a priori* estimation of the rupture speed. Bouchon *et al.* (2010) observed the fault rupture surface of several earthquakes with supershear ruptures and concluded that the rupture may propagate at a supershear speed only when the geometry of the fault is simple. Besides, Manighetti *et al.* (2007) and Radiguet *et al.* (2009) analyzed stress drop, another important source parameter, with respect to the so-called maturity of faults. Maturity includes fault features such as age, length, and cumulative displacement on the fault. The authors conclude that mature faults are associated with low stress drop. Finally, Causse and Song (2015) propose that average stress drop and average rupture velocity may not be independent but anticorrelated, and propose joint distributions of these parameters. *A priori* knowledge of the stress drop may then also help constrain the rupture velocity for *a priori* estimations of the pulse periods.

Conclusions

This article presents a simple equation to predict the period of the velocity pulses that can be observed in the near-fault region and in the forward rupture direction. This equation is based on a few basic parameters: (1) the location of the station with respect to the rupture, (2) the velocity of the rupture propagation, and (3) the rise time and the shear-wave velocity of the medium around the fault. Our approach is first validated by analyzing a suite of synthetic velocity time series of strike-slip extended ruptures. The velocity pulse periods are computed from the Baker (2007) algorithm, based on wavelet transform. This analysis shows that (1) the pulse period is sensitive to the rupture length toward the station rather than the whole length of the fault; (2) the pulse period is not sensitive to the heterogeneity of the slip distribution on the fault plane; and (3) the value of the pulse period as computed from the wavelet analysis can differ from the real duration of the directivity pulse at stations located next to or beyond the rupture termination.

Our equation is then tested on a dataset build from the NGA-West2 database, consisting of 110 observations of pulses periods from 10 strike-slip events and 6 non-strike-slip events. The standard deviation of the natural logarithm residuals between observations and prediction is ~0.5, and the correlation coefficient between observations and predictions is 0.84 (0.86 considering strike-slip events only and 0.68 for non-strike-slip events). This indicates that despite significant discrepancies observed at some stations, our simple model reproduces the spatial variability of the pulse periods recorded during an earthquake fairly well, especially for strike-slip events. As mentioned above, some of these discrepancies can be explained by unsuitable values of the rupture velocity, complexity of the fault geometry, or inadequacy between the pulse duration and the value of the pulse period, which depends on the technique used to extract the pulse. Note that some of these discrepancies may also be explained by the variability of the site conditions, which is not considered in equation (1). Overall, soil sites are generally characterized by larger values of the pulse period than rock sites (e.g., Somerville, 2003; Bray and Rodriguez-Marek, 2004; Cork *et al.*, 2016).

Finally, it is important to mention that proper *a priori* estimations of the pulse period for a potential future earthquake rely on a proper *a priori* knowledge of the location of the hypocenter, the rupture velocity, and the rise time.

Data and Resources

The Next Generation Attenuation-West2 Project (NGA-West2) database was searched using http://peer.berkeley.edu/ngawest2/databases/ (last accessed March 2016). The rupture speed values reported by several finite-source inversion models were searched using http://equake-rc.info/SRCMOD/ (last accessed March 2016). The pulse periods of the synthetic velocity time series were computed using the Baker (2007) algorithm (MATLAB computer code available at https://github.com/shreyshahi/PulseClassification, last accessed June 2015).

Acknowledgments

We thank an anonymous reviewer and Paul Spudish for valuable comments and insight that improved the article. This study has been partially supported by Université Grenoble Alpes (AGIR-POLE-PAGE project), by Institut National des Sciences de l'Univers (Centre National de la Recherche Scientifique [CNRS]-Tellus-ALEAS project), by the STREST project (Seventh Framework Programme [FP7/2007-2013] under Grant Agreement Number 603389), and by the IRD young research united on Mass Movement, Seismic Hazard and Variability JEAI SAMMOVA (2015–2017) funded by Institute de Recherche pour le Développement (IRD).

References

Alavi, B., and H. Krawinkler (2001). Effects of near-fault ground motions on frame structures, *Report No. 138*, John A. Blume Earthquake Engineering Center.

Anderson, J. C., and V. V. Bertero (1987). Uncertainties in establishing design earthquakes, *Am. Soc. Civil Eng.* **113,** no. 8, 1709–1724.

Archuleta, R. J. (1984). A faulting model for the 1979 Imperial Valley earthquake, *J. Geophys. Res.* **89,** no. B6, 4559–4585, doi: 10.1029/JB089iB06p04559.

Baker, J. W. (2007). Quantitative classification of near-fault ground motions using wavelet analysis, *Bull. Seismol. Soc. Am.* **97,** no. 5, 1486–1501, doi: 10.1785/0120060255.

Bernard, P., and D. Baumont (2005). Shear Mach wave characterization for kinematic fault rupture models with constant supershear rupture velocity, *Geophys. J. Int.* **162,** no. 2, 431–447, doi: 10.1111/j.1365-246X.2005.02611.x.

Biggs, J. M. (1964). *Introduction to Structural Dynamics*, McGraw-Hill, New York, New York.

Bouchon, M. (1981). A simple method to calculate Green's functions for elastic layered media, *Bull. Seismol. Soc. Am.* **71,** no. 4, 959–971.

Bouchon, M., D. Hatzfeld, J. A. Jackson, and E. Haghshenas (2006). Some insight on why Bam (Iran) was destroyed by an earthquake of relatively moderate size, *Geophys. Res. Lett.* **33,** no. 9, doi: 10.1029/2006GL025906.

Bouchon, M., H. Karabulut, M.-P. Bouin, J. Schmittbuhl, M. Vallee, R. J. Archuleta, and D. Marsan (2010). Faulting characteristics of supershear earthquakes, *Tectonophysics* **493,** nos. 3/4, 244–253, doi: 10.1016/j.tecto.2010.06.011.

Bray, J. D., and A. Rodriguez-Marek (2004). Characterization of forward-directivity ground motions in the near-fault region, *Soil Dynam. Earthq. Eng.* **24,** 815–828, doi: 10.1016/j.soildyn.2004.05.001.

Causse, M., and S. G. Song (2015). Are stress drop and rupture velocity of earthquakes independent? Insight from observed ground motion variability, *Geophys. Res. Lett.* **42,** no. 18, 7383.

Causse, M., E. Chaljub, F. Cotton, C. Cornou, and P.-Y. Bard (2009). New approach for coupling k^{-2} and empirical Green's functions: Application to the blind prediction of broad-band ground motion in the Grenoble basin, *Geophys. J. Int.* **179,** no. 3, 1627–1644, doi: 10.1111/j.1365-246X.2009.04354.x.

Cho, I., and I. Nakanishi (2000). Investigation of the three-dimensional fault geometry ruptured by the 1995 Hyogo-Ken Nanbu earthquake using strong-motion and geodetic data, *Bull. Seismol. Soc. Am.* **90,** no. 2, 450–467.

Cork, T. G., J. H. Kim, G. P. Mavroeidis, J. K. Kim, B. Halldorsson, and A. S. Papageorgiou (2016). Effects of tectonic regime and soil conditions on the pulse period of near-fault ground motions, *Soil Dynam. Earthq. Eng.* **80,** 102–118, doi: 10.1016/j.soildyn.2015.09.011.

Custodio, S., P. Liu, and R. J. Archuleta (2005). The 2004 M_w 6.0 Parkfield, California, earthquake: Inversion of near-source ground motion using multiple data sets, *Geophys. Res. Lett.* **32,** no. 23, doi: 10.1029/2005GL024417.

Guo, Y., K. Koketsu, and T. Ohno (2013). Analysis of the rupture process of the 1995 Kobe earthquake using a 3D velocity structure, *Earth Planets Space* **65,** no. 12, 1581–1586, doi: 10.5047/eps.2013.07.006.

Hall, J. F., T. H. Heaton, M. W. Halling, and D. J. Wald (1995). Near-source ground motion and its effects on flexible buildings, **11,** 569–605.

Heaton, T. H. (1990). Evidence for and implications of self-healing pulses of slip in earthquake rupture, *Phys. Earth Planet. In.* **64,** no. 1, 1–20.

Horikawa, H., K. Hirahara, Y. Umeda, M. Hashimoto, and F. Kusano (1996). Simultaneous inversion of geodetic and strong-motion data for the source process of the Hyogo-ken Nanbu, Japan, earthquake, *J. Phys. Earth* **44,** no. 5, 455–471.

Hubbard, D. T., and G. P. Mavroeidis (2011). Damping coefficients for near-fault ground motion response spectra, *Soil Dynam. Earthq. Eng.* **31,** 401–417, doi: 10.1016/j.soildyn.2010.09.009.

Ide, S., M. Takeo, and Y. Yoshida (1996). Source process of the 1995 Kobe earthquake; determination of spatio-temporal slip distribution by Bayesian modeling, *Bull. Seismol. Soc. Am.* **86,** no. 3, 547–566.

Koketsu, K., S. Yoshida, and H. Higashihara (1998). A fault model of the 1995 Kobe earthquake derived from the GPS data on the Akashi Kaikyo Bridge and other datasets, *Earth Planets Space* **50,** no. 10, 803–811.

Liossatou, E., and M. N. Fardis (2016). Near-fault effects on residual displacements of RC structures, *Earthq. Eng. Struct. Dynam.* **45,** no. 9, 1391–1409, doi: 10.1002/eqe.2712.

Mai, P. M., and K. K. S. Thingbaijam (2014). SRCMOD: An online database of finite-fault rupture models, *Seismol. Res. Lett.* **85,** 1348–1357.

Manighetti, I., M. Campillo, S. Bouley, and F. Cotton (2007). Earthquake scaling, fault segmentation, and structural maturity, *Earth Planet. Sci. Lett.* **253,** nos. 3/4, 429–438, doi: 10.1016/j.epsl.2006.11.004.

Mavroeidis, G. P., and A. Papageorgiou (2003). A mathematical representation of near-fault ground motions, *Bull. Seismol. Soc. Am.* **93,** 1099–1131.

Mavroeidis, G. P., and A. S. Papageorgiou (2010). Effect of fault rupture characteristics on near-fault strong ground motions, *Bull. Seismol. Soc. Am.* **100,** no. 1, 37–58, doi: 10.1785/0120090018.

Mavroeidis, G. P., G. Dong, and A. Papageorgiou (2004). Near-fault ground motions, and the response of elastic and inelastic single-degree-of-freedom (SDOF) systems, *Earthq. Eng. Struct. Dynam.* **33,** no. 9, 1023–1049, doi: 10.1002/eqe.391.

Radiguet, M., F. Cotton, I. Manighetti, M. Campillo, and J. Douglas (2009). Dependency of near-field ground motions on the structural maturity of the ruptured faults, *Bull. Seismol. Soc. Am.* **99,** no. 4, 2572–2581, doi: 10.1785/0120080340.

Ruiz-Garcia, J. (2011). Inelastic displacement ratios for seismic assessment of structures subjected to forward-directivity near-fault ground motions, *J. Earthq. Eng.* **15,** no. 3, 449–468, doi: 10.1080/13632469.2010.498560.

Sekiguchi, H., K. Irikura, and T. Iwata (2000). Fault geometry at the rupture termination of the 1995 Hyogo-ken Nanbu earthquake, *Bull. Seismol. Soc. Am.* **90,** no. 1, 117–133.

Shahi, S. K., and J. W. Baker (2011). An empirically calibrated framework for including the effects of near-fault directivity in probabilistic seismic hazard analysis, *Bull. Seismol. Soc. Am.* **101,** no. 2, 742–755, doi: 10.1785/0120100090.

Somerville, P. G. (1998). Development of an improved representation of near fault ground motions, *SMIP98 Seminar on Utilization of Strong-Motion Data*, Vol. 15, September 1998, Oakland, California.

Somerville, P. G. (2003). Magnitude scaling of the near fault rupture directivity pulse, *Phys. Earth Planet. In.* **137,** 201–212, doi: 10.1016/S0031-9201(03)00015-3.

Somerville, P., K. Irikura, R. P. Graves, S. Sawada, D. J. Wald, N. Abrahamson, Y. Iwasaki, T. Kagawa, N. Smith, and A. Kowada (1999). Characterizing crustal earthquake slip models for the prediction of strong ground motion, *Seismol. Res. Lett.* **70,** no. 1, 59–80.

Somerville, P. G., N. F. Smith, R. W. Graves, and N. A. Abrahamson (1997). Modification of empirical strong ground motion attenuation relations to include the amplitude and duration effects of rupture directivity, *Seismol. Res. Lett.* **68,** no. 1, 199–222.

Spudich, P., and B. S. J. Chiou (2008). Directivity in NGA earthquake ground motions: Analysis using isochrone theory, *Earthq. Spectra* **24,** no. 1, 279–298, doi: 10.1193/1.2928225.

Thio, H. K., and H. Kanamori (1996). Source complexity of the 1994 Northridge earthquake and its relation to aftershock mechanisms, *Bull. Seismol. Soc. Am.* **86,** no. 1, 84–92.

Twardzik, C., R. Madariaga, S. Das, and S. Custodio (2012). Robust features of the source process for the 2004 Parkfield, California, earthquake from strong-motion seismograms, *Geophys. J. Int.* **191,** no. 3, 1245–1254, doi: 10.1111/j.1365-246X.2012.05653.x.

Veletsos, A., N. Newmark, and C. V. Chelapati (1965). Deformation spectra for elastic and elastoplastic systems subjected to ground shock and earthquake motions, *Proc. of the 3rd World Conference on Earthquake Engineering*, Vol. 2, 663–682.

Wald, D. J. (1996). Slip history of the 1995 Kobe, Japan, earthquake determined from strong motion, teleseismic, and geodetic data, *J. Phys. Earth* **44,** no. 5, 489–503.

Yoshida, S., K. Koketsu, B. Shibazaki, T. Sagiya, T. Kato, and Y. Yoshida (1996). Joint inversion of near- and far-field waveforms and geodetic

data for the rupture process of the 1995 Kobe earthquake, *J. Phys. Earth* **44,** no. 5, 437–454.

Zeng, Y., and J. Anderson (2000). Evaluation of numerical procedures for simulating near-fault long-period ground motions using Zeng method, *Report 2000/01 to the PEER Utilities Program*, Pacific Earthquake Engineering Research Center.

Appendix

Table A1 represents the dataset of analysed pulse periods described by the Next Generation Attenuation-West2 Project (NGA-West2) database.

Table A1
Dataset of Pulse Periods Considered in This Study, Build from the Next Generation Attenuation-West2 Project (NGA-West2) Database

	Earthquake	Station Name	*HypD**	*ClstD*†	*D*‡	T_p (NGA)§
1	Coyote Lake	Gilroy Array number 3	12.49	7.42	6.46	1.155
2	Coyote Lake	Gilroy Array number 6	9.12	3.11	6.46	1.232
3	Coyote Lake	Gilroy Array number 4	11.08	5.7	6.46	1.351
4	Coyote Lake	Gilroy Array number 2	13.55	9.02	6.46	1.463
6	Parkfield	Cholame 3E	14.37	5.55	11.46	0.518
7	Parkfield	Stone Corral 1E	10.82	3.79	8.61	0.574
8	Parkfield	Cholame 4W	14.74	4.23	11.46	0.7
9	Parkfield	Slack Canyon	32.55	2.99	30.52	0.854
10	Parkfield	Cholame 3W	14.62	3.63	11.46	1.022
11	Parkfield	Cholame 2WA	14.10	3.01	11.46	1.078
12	Parkfield	Fault Zone 9	12.86	2.85	11.38	1.134
13	Parkfield	Fault Zone 1	11.67	2.51	10.09	1.19
14	Parkfield	Fault Zone 12	13.66	2.65	12.30	1.19
15	Parkfield	EADES	12.83	2.85	11.32	1.218
16	Parkfield	Cholame 1E	14.02	3	11.46	1.33
18	Morgan Hill	Coyote Lake Dam–SW	25.98	0.53	25.82	1.071
19	Morgan Hill	Gilroy Array number 6	37.32	9.87	27.69	1.232
21	Imperial Valley	Agrarias	10.30	0.65	10.28	2.338
22	Imperial Valley	El Centro–Me Geot	21.84	0.07	21.84	3.423
23	Imperial Valley	El Centro Array number 6	29.22	1.35	29.19	3.773
24	Imperial Valley	El Centro Array number 5	29.53	3.95	29.26	4.13
25	Imperial Valley	El Centro Array number 7	29.38	0.56	29.34	4.375
26	Imperial Valley	Brawley Airport	44.29	10.42	39.05	4.396
27	Imperial Valley	EC County Center FF	30.73	7.31	29.41	4.417
28	Imperial Valley	El Centro Array number 3	30.33	12.85	27.47	4.501
29	Imperial Valley	El Centro Array number 10	30.46	8.6	28.70	4.515
30	Imperial Valley	El Centro Array number 4	28.90	7.05	28.03	4.788
31	Imperial Valley	Holtville Post Office	22.16	7.5	20.85	4.823
32	Imperial Valley	El Centro Diff. Array	29.00	5.09	28.23	6.265
34	Superstition Hills	Kornbloom Road	21.27	18.48	10.54	2.128
35	Superstition Hills	Parachute Test Site	18.35	0.95	18.33	2.394
37	Bam, Iran	Bam	13.94	1.7	13.39	2.023
39	Kobe, Japan	KJMA	25.58	0.96	25.36	1.092
40	Kobe, Japan	Takatori	22.19	1.47	21.88	1.554
41	Kobe, Japan	Takarazuka	42.55	0.27	42.47	1.806
42	Kobe, Japan	Port Island (83 m)	26.28	3.31	26	2.534
43	Kobe, Japan	Port Island (0 m)	26.28	3.31	25.74	2.828
45	Duzce, Turkey	Bolu	43.58	12.04	32.61	0.882
46	Duzce, Turkey	IRIGM 487	26.72	2.65	24.67	10.052
48	Landers	Lucerne	44.58	2.19	48.06	5.124
49	Landers	Yermo Fire Station	86.28	23.62	66.18	7.504
50	Landers	Barstow	95.02	34.86	66.18	9.128
52	Kocaeli, Turkey	Yarimca	25.07	4.83	24.35	4.949
53	Kocaeli, Turkey	İzmit	16.86	7.21	15.41	5.369
54	Kocaeli, Turkey	Gebze	49.68	10.92	48.40	5.992
55	Kocaeli, Turkey	Arcelik	56.02	13.49	49.16	7.791
57	San Fernando	Pacoima Dam (up. left)	17.60	1.81	13.44	1.638
59	Northridge	Pacoima Dam (downstr)	26.85	7.01	19.88	0.588
60	Northridge	Pacoima Kagel Canyon	26.04	7.26	19.88	0.728
61	Northridge	Pacoima Dam (up. left)	26.85	7.01	19.88	0.84
62	Northridge	LA–Sepulveda VA H	19.45	8.44	17.54	0.931

(*continued*)

Table A1 (*Continued*)

	Earthquake	Station Name	*HypD**	*ClstD*†	*D*‡	T_p (NGA)§
63	Northridge	Pardee–SCE	31.05	7.46	24.08	1.232
64	Northridge	Rinaldi Receiving Sta	20.62	6.5	19.55	1.246
65	Northridge	Newhall–Fire Sta	26.78	5.92	21.50	1.372
66	Northridge	LA Dam	21.10	5.92	19.50	1.617
67	Northridge	Sylmar–OV Med FF	24.24	5.3	19.55	2.436
68	Northridge	Newhall–W P C Rd.	27.76	5.48	24.08	2.982
69	Northridge	Sylmar–Converter Sta	21.87	5.35	19.54	2.982
70	Northridge	Jensen Filter Plant Adm	21.78	5.43	19.58	3.157
71	Northridge	Sylmar–Conv Sta East	22.16	5.19	19.51	3.528
72	Northridge	Jensen Filter Plant Gen	21.80	5.43	19.60	3.535
74	Loma Prieta	Los Gatos–Lex. Dam	26.83	5.02	23.60	1.568
75	Loma Prieta	Gilroy–Historic Building	33.10	10.97	24.71	1.638
76	Loma Prieta	Gilroy Array number 2	34.52	11.07	24.71	1.729
77	Loma Prieta	Gilroy Array number 3	35.94	12.82	24.71	2.639
78	Loma Prieta	Saratoga–Aloha Avenue	32.35	8.5	24.74	4.571
79	Loma Prieta	Saratoga–W V Coll.	32.20	9.31	24.74	5.649
81	Cape Mendocino	Centerville Beach, N F	29.58	18.31	13	1.967
82	Cape Mendocino	Petrolia	10.52	8.18	6.67	2.996
83	Cape Mendocino	Bunker Hill FAA	21.86	12.24	12	5.362
85	Tabas, Iran	Tabas	55.54	2.05	55.08	6.188
87	Chi-Chi, Taiwan	CHY006	41.26	9.76	33.54	2.5704
88	Chi-Chi, Taiwan	TCU	37.07	5.16	36.31	4.508
89	Chi-Chi, Taiwan	TCU076	17.91	2.74	15.73	4.732
90	Chi-Chi, Taiwan	TCU075	22.16	0.89	21.68	4.998
91	Chi-Chi, Taiwan	TCU029	79.60	28.04	58.92	5.285
92	Chi-Chi, Taiwan	CHY101	32.95	9.94	32.08	5.341
93	Chi-Chi, Taiwan	TCU036	68.28	19.83	50.77	5.383
94	Chi-Chi, Taiwan	TCU065	27.85	0.57	27.93	5.74
95	Chi-Chi, Taiwan	WGK	32.95	9.94	32.08	5.74
96	Chi-Chi, Taiwan	TCU031	80.49	30.17	58.92	5.929
97	Chi-Chi, Taiwan	TCU040	69.51	22.06	50.77	6.433
98	Chi-Chi, Taiwan	TCU063	36.35	9.78	28.21	6.552
99	Chi-Chi, Taiwan	CHY024	25.39	9.62	17.92	6.65
100	Chi-Chi, Taiwan	TCU104	49.93	12.87	45.87	7.189
101	Chi-Chi, Taiwan	TCU059	53.97	17.11	45.87	7.784
102	Chi-Chi, Taiwan	NST	89.20	38.42	57.86	7.875
103	Chi-Chi, Taiwan	TCU046	69.35	16.74	58.92	8.043
104	Chi-Chi, Taiwan	TCU082	37.07	5.16	36.31	8.099
105	Chi-Chi, Taiwan	TCU026	106.51	56.12	57.50	8.372
106	Chi-Chi, Taiwan	TCU064	59.68	16.59	49.82	8.456
107	Chi-Chi, Taiwan	TCU103	53.04	6.08	50.77	8.687
108	Chi-Chi, Taiwan	TCU034	88.24	35.68	58.92	8.869
109	Chi-Chi, Taiwan	TCU136	49.40	8.27	45.87	8.8816
110	Chi-Chi, Taiwan	TCU056	40.53	10.48	37.48	8.939
111	Chi-Chi, Taiwan	TCU033	93.41	40.88	58.92	8.974
112	Chi-Chi, Taiwan	TCU128	63.80	13.13	58.92	9.023
113	Chi-Chi, Taiwan	NSY	63.80	13.13	58.92	9.163
114	Chi-Chi, Taiwan	TCU039	71.95	19.89	58.92	9.331
115	Chi-Chi, Taiwan	TCU045	77.91	26	58.92	9.338
116	Chi-Chi, Taiwan	TCU038	73.55	25.42	50.77	9.576
117	Chi-Chi, Taiwan	TCU102	46.26	1.49	46.78	9.632
118	Chi-Chi, Taiwan	TCU049	39.73	3.76	39.77	10.22
119	Chi-Chi, Taiwan	TCU101	45.75	2.11	45.87	10.318
120	Chi-Chi, Taiwan	TCU051	39.35	7.64	37.68	10.381
121	Chi-Chi, Taiwan	TCU087	56.21	6.98	58.92	10.395
122	Chi-Chi, Taiwan	TCU052	40.38	0.66	41.70	11.956
123	Chi-Chi, Taiwan	TCU068	48.52	0.32	50.96	12.285
124	Chi-Chi, Taiwan	TCU047	86.76	35	58.92	12.313
125	Chi-Chi, Taiwan	TCU053	41.97	5.95	41.34	13.118

*Hypocenter distance in kilometers.

†Closest distance in kilometers.

‡Distance between the hypocenter and the closest distance from the station to the fault rupture area in kilometers.

§Pulse period in seconds.

Université Grenoble Alpes, CNRS, IRD, IFSTTAR, ISTerre
CS 40700
38000 Grenoble, Cedex 9
France
rose-marie.fayjaloun@univ-grenoble-alpes.fr
(R.F., M.C., C.V., C.C.)

GFZ German Research Center for Geosciences
Telegrafenberg
14473 Potsdam
Germany
(F.C.)

Manuscript received 26 June 2016;
Published Online 27 December 2016